MNRAS **431,** 2453–2463 (2013)
Advance Access publication 2013 March 21
doi:10.1093/mnras/stt340

# Performing a stellar autopsy using the radio-bright remnant of SN 1996cr

C. Meunier,[1⋆] F. E. Bauer,[1,2,3⋆] V. V. Dwarkadas,[4] B. Koribalski,[5] B. Emonts,[5] R. W. Hunstead,[6] D. Campbell-Wilson,[6] C. Stockdale[7] and S. J. Tingay[8]

[1]*Pontificia Universidad Católica de Chile, Departamento de Astronomía y Astrofísica, Casilla 306, Santiago 22, Chile*
[2]*Space Science Institute, 4750 Walnut Street, Suite 205, Boulder, CO 80301, USA*
[3]*Columbia Astrophysics Laboratory, 550 W 120th Street, Columbia University, NY 10027, USA*
[4]*Department of Astronomy and Astrophysics, U Chicago, 5640 S Ellis Ave, Chicago, IL 60637, USA*
[5]*Australia Telescope National Facility, CSIRO Astronomy and Space Science, PO Box 76, Epping, NSW 1710, Australia*
[6]*Sydney Institute for Astronomy, School of Physics, University of Sydney, NSW 2006, Australia*
[7]*Department of Physics, Marquette University, PO Box 1881, Milwaukee, WI 53201-1881, USA*
[8]*International Centre for Radio Astronomy Research, Curtin University, Bentley 6102, WA, Australia*

Accepted 2013 February 21. Received 2013 February 20; in original form 2012 August 29

## ABSTRACT

We present newly reduced archival radio observations of SN 1996cr in the Circinus Galaxy from the Australia Telescope Compact Array and the Molonglo Observatory Synthesis Telescope, and attempt to model its radio light curves using recent hydrodynamical simulations of the interaction between the supernova (SN) ejecta and the circumstellar material (CSM) at X-ray wavelengths. The radio data within the first 1000 d show clear signs of free–free absorption (FFA), which decreases gradually and is minimal above 1.4 GHz after day ∼3000. Constraints on the FFA optical depth provide estimates of the CSM free electron density, which allows insight into the ionization of SN 1996cr's CSM and offers a test on the density distribution adopted by the hydrodynamical simulation. The intrinsic spectral index of the radiation shows evidence for spectral flattening, which is characterized by $\alpha = 0.852 \pm 0.002$ at day 3000 and a decay rate of $\Delta\alpha = -0.014 \pm 0.001$ yr$^{-1}$. The striking similarity in the spectral flattening of SN 1987A, SN 1993J and SN 1996cr suggests this may be a relatively common feature of SNe/CSM shocks. We adopt this spectral index variation to model the synchrotron radio emission of the shock, and consider several scalings that relate the parameters of the hydrodynamical simulation to the magnetic field and electron distribution. The simulated light curves match the large-scale features of the observed light curves, but fail to match certain tightly constraining sections. This suggests that simple energy density scalings may not be able to account for the complexities of the true physical processes at work, or alternatively, that the parameters of the simulation require modification in order to accurately represent the surroundings of SN 1996cr.

**Key words:** methods: numerical – circumstellar matter – supernovae: general – supernovae: individual: SN 1996cr – stars: winds, outflows.

## 1 INTRODUCTION

Radio and X-ray emission arising from remnants of supernovae (SNe) provide rich information about the ongoing interaction between the SN ejecta and the circumstellar material (CSM). The fact that SN ejecta expand approximately two to three orders of magnitude faster than the slower moving progenitor stellar wind ensures that, in a matter of decades, the ejecta will have swept up and revealed information on tens to thousands of years of stellar evolution leading up to the explosion; thus, providing an alternate window for studying the evolution and classification of the progenitor stars (Chevalier & Fransson 1994).

An analytical model of the emission from radio SNe (RSNe) was developed by Chevalier (1982, hereafter the 'standard' model), in which the SN ejecta and CSM density profiles are described as power laws in radius, and the evolution of the shock front is characterized by a self-similar solution in which the shock radii expand as power laws in time. The interaction between the SN ejecta and the CSM leads to the formation of a contact discontinuity, bounded by a forward shock travelling into the CSM and a reverse shock moving back into the ejecta relative to the contact discontinuity. The radio emission arising from these two shocks is typically characterized as synchrotron radiation from ultrarelativistic electrons accelerated

⋆E-mail: clmeunie@uc.cl (CM); fbauer@astro.puc.cl (FEB)

at the shock front (Duffy, Ball & Kirk 1995; Reynolds 2008). If the energy density of the magnetic field as well as the relativistic particles can be assumed as proportional to the thermal energy density, then this treatment provides a simple formula for the radio emission. This has been successful in describing the radio light curves of SNe exploding into simple red supergiant (RSG) type winds, where the emission decreases as a power law in time (Weiler et al. 2002). It fails, however, to account for the light curves of RSNe which do not decrease in power-law fashion, and therefore where the CSM has presumably been altered by perhaps a binary companion, or by various evolutionary stages both on or after the main sequence (cf. table 4 in Soderberg et al. 2006).

The late-stage evolution of stars more massive than $\sim$20 $M_{\odot}$ should extend beyond the initial post-main sequence RSG phase into yellow or blue supergiant (BSG), luminous blue variable and/or Wolf–Rayet (WR) phases (e.g. Lamers, Maeder & Schmutz 1991; Stothers & Chin 1996). The relatively high mass-loss rates and/or wind velocities often present during these later phases (e.g. Nugis & Lamers 2000; Vink et al. 2011) can result in stellar winds with enough momentum to sweep up ambient material deposited by winds during previous evolutionary stages of the star, creating a low-density cavity bordered by a dense shell of swept-up material (Weaver et al. 1977). Once the progenitor explodes, the ejecta expand within this complex CSM, which is not represented by a power-law density profile, and for which the standard model, which assumes self-similar shock expansion, is not applicable (Chevalier & Liang 1989; Tenorio-Tagle et al. 1990, 1991; Dwarkadas 2005, 2007a). We *must* therefore model the ejecta–CSM interaction through hydrodynamical simulations using prescribed ejecta and CSM density profiles. The resulting hydrodynamical quantities (pressure, density and temperature) can then be input to radiative transfer equations to simulate the radio light curves and spectra of the SN (e.g. Mioduszewski, Dwarkadas & Ball 2001; Martí-Vidal et al. 2011).

We employ a simplified version of this method to study the radio light curve of SN 1996cr, located in the Circinus Galaxy ($\sim$3.8 Mpc; Freeman et al. 1977; Koribalski et al. 2004), which exploded around 1996 and was confirmed as a Type IIn SN by Bauer et al. (2007) $\sim$11 yr later. Serendipitous archival data provide a crude picture of the explosion dynamics and the late evolutionary history of the progenitor (see, e.g. Bauer et al. 2008 and references therein). In behaviour reminiscent of SN 1987A (Park et al. 2005; Zanardo et al. 2010), SN 1996cr shows an increase of X-ray and radio luminosity in the years following the initial explosion. Dwarkadas, Dewey & Bauer (2010) studied SN 1996cr through hydrodynamic simulations of the ejecta–CSM interaction, from which they accurately reproduced the X-ray light curves and spectra, and in doing so derived valuable constraints on the CSM distribution: SN 1996cr exploded in a low-density medium and expanded freely before interacting with a dense shell of material at about 0.04 pc, which is thought to be the result of the interaction between fast winds of either a BSG or WR star and a slower wind, possibly from a previous RSG stage which is not yet well constrained by observations.

In this work, we provide an observational update on the radio evolution of SN 1996cr, and attempt to compute the radio light curves from the hydrodynamic simulation in Dwarkadas et al. (2010). The constraints on the simulation parameters came primarily from the observed X-ray light curves and spectra. However, there are no X-ray detections prior to year 2000, and only a few relatively weak soft X-ray upper limits before that (Bauer et al. 2008; Dwarkadas et al. 2010). Thus, for the epoch when the shock is thought to have first encountered the dense shell in 1997, there are no direct thermal constraints on the density of the inner cavity implemented in the simulation. Radio detections of SN 1996cr start as early as mid-1996, and could provide constraints on the CSM density during this period, since both the X-ray and radio emissions can be ultimately related to the density of the emitting region. Probing the CSM density of the inner boundary of the shell and possibly even the initial cavity using the radio light curve may ultimately help to refine some of the uncertainties in the hydrodynamic simulation, give us a better picture of the CSM structure and thereby provide more information about the progenitor star and its evolution.

This study is organized as follows. Radio data and reduction methods are detailed in Section 2. In Section 3, we characterize the observational properties of SN 1996cr and outline how we translate the hydrodynamic simulation into a radio emission model. In Section 4, we explore the H II region surrounding SN 1996cr and present the simulated radio light curves. Finally, in Section 5 we discuss the results and implications of this study. In this paper, we adopt the explosion epoch of 1995.6 determined in Bauer et al. (2008). All errors are quoted at $1\sigma$ unless otherwise stated.

## 2 RADIO OBSERVATIONS

Bauer et al. (2008) provide radio data up to 2007. However, since more data exist for comparison, and some of the data presented in Bauer et al. (2008) were rereduced to clean up artefacts and incorporate a larger array of calibration data, we detail the data reduction procedures here. The data presented here supersede those of Bauer et al. (2008).

Numerous observations of the Circinus Galaxy exist from studies at radio wavelengths spanning 1995 to 2011 (e.g., Elmouttie et al. 1995; Greenhill et al. 1997; Phillips et al. 1998; Jones et al. 1999; McCallum et al. 2005, 2009; Wilson et al. 2011). These were retrieved from the Australia Telescope Compact Array (ATCA) archive[1] and were reduced with MIRIAD (v4.0.5 and v20110616) following the procedures outlined in the ATNF Miriad User Manual.[2] Fluxes for SN 1996cr are presented in Table 1 and Fig. 1.

For the 1.4, 2.4, 4.8 and 8.5 GHz observations, the 'primary' flux calibrator was typically PKS B1934−638, with approximate flux densities of 14.9, 11.6, 5.8 and 2.8 Jy, respectively. For 15–25 GHz observations the 'primary' flux calibrators were either PKS B1934−638 (0.7–1.2 Jy) or PKS B1921−293 (10–25 Jy). For the 36 and 89 GHz observations, the primary calibrators were Mars and Uranus.

The secondary calibrators, which served as the gain, bandpass and phase calibrators for the Circinus Galaxy, varied from observation to observation and were variable in time, and include (in descending order of use) sources PKS B1921−293 (bandpass, alternate 22.5 GHz flux), PKS B0823−500 (bandpass, alternate flux), PMN J1355−6326 (phase), PMN J1417−5950 (phase), PKS B1329−665 (bandpass, phase), PKS B1718−649 (phase), PKS B1549−790 (phase), PMN J1047−6217 (phase), PKS B1104−445 (phase), PKS B1424−418 (phase), PKS B1610−771 (phase), PMN J1342−5828 (phase) and PKS B1236−684 (phase). Flux densities for the calibrators are provided in the Appendix. To cross-check our flux calibration, the flux densities of the secondary calibrators were compared to their average or interpolated

[1] http://atoa.atnf.csiro.au/

[2] http://www.atnf.csiro.au/computing/software/miriad/

**Table 1.** ATCA Radio observations.

| Obs. date | Days from explosion | Obs. ID | Array | *W* band | | $K_a$ band | | *K* band | | *X* band | | *C* band | | *S* band | | *L* band | | UHF | |
|---|---|---|---|---|---|---|---|---|---|---|---|---|---|---|---|---|---|---|---|
| | | | | $\nu$ | $S_\nu$ | $\nu$ | $S_\nu$ | $\nu$ | $S_\nu$ | $\nu$ | $S_\nu$ | $\nu$ | $S_\nu$ | $\nu$ | $S_\nu$ | $\nu$ | $S_\nu$ | | |
| (1) | (2) | (3) | (4) | (5) | (6) | (7) | (8) | (9) | (10) | (11) | (12) | (13) | (14) | (15) | (16) | (17) | (18) | (19) | (20) |
| 1995-03-03 | −120 | C204a | 750A | – | – | – | – | – | – | 8640 | <0.3 | 4800 | <0.6 | – | – | – | – | – | – |
| 1995-03-03 | −120 | C204a | 750A | – | – | – | – | – | – | 8640 | <0.3 | 4800 | <0.4 | – | – | – | – | – | – |
| 1995-03-30 | −93 | C363 | 1.5A | – | – | – | – | – | – | – | – | – | – | – | – | 1418 | <6.6 | – | – |
| 1995-04-16 | −76 | C418 | 6C | – | – | – | – | – | – | – | – | – | – | 2768 | <1.1 | 1418 | <1.2 | – | – |
| 1995-05-27 | −35 | C204a | 1.5B | – | – | – | – | – | – | 8640 | <0.3 | 4800 | <0.2 | – | – | – | – | – | – |
| 1995-05-27 | −35 | C204a | 1.5B | – | – | – | – | – | – | 8640 | <0.3 | 4800 | <0.5 | – | – | – | – | – | – |
| 1995-06-07 | −24 | C204a | 750C | – | – | – | – | – | – | 8640 | <0.8 | 4800 | <0.3 | – | – | – | – | – | – |
| 1995-06-07 | −24 | C204a | 750C | – | – | – | – | – | – | 8640 | <0.3 | 4800 | <0.2 | – | – | – | – | – | – |
| 1995-07-27 | 26 | C204c | 6C | – | – | – | – | – | – | – | – | – | – | 2368 | <1.3 | 1376 | <3.4 | – | – |
| 1995-08-03 | 33 | C363 | 375 | – | – | – | – | – | – | – | – | – | – | – | – | 1418 | <16.7 | – | – |
| 1996-02-06 | 220 | CT09 | 750B | – | – | – | – | – | – | – | – | – | – | – | – | 1664 | <1.5 | – | – |
| 1996-08-01 [(1)] | 397 | C466 | 6C | – | – | – | – | – | – | 8640 | $0.5 \pm 0.0$ | 4800 | <1.0 | – | – | – | – | – | – |
| 1996-12-05 [(2)] | 523 | C505 | 365 | – | – | – | – | – | – | – | – | – | – | 2368 | <0.4 | 1384 | <0.7 | – | – |
| 1996-12-15 [(2)] | 533 | C586 | 6D | – | – | – | – | – | – | 8512 | $1.9 \pm 0.1$ | 4928 | $1.8 \pm 0.1$ | – | – | – | – | – | – |
| 1996-12-15 [(2)] | 533 | C586 | 6D | – | – | – | – | – | – | 8512 | $2.3 \pm 0.1$ | 4928 | $1.8 \pm 0.1$ | – | – | – | – | – | – |

*Note*. The full table is available in the online journal. Column 1: starting date of observation. Numbers in parenthesis indicate epochs whose data were combined, as described in Section 3.2. Column 2: days from explosion date. Column 3: observing programme ID. Column 4: array configuration. Columns 5, 7, 9, 11, 13, 15, 17, and 19: mean frequency of observed band in units of MHz. Columns 6, 8, 10, 12, 14, 16, 18, and 20: integrated flux densities, as determined from IMFIT, or $3\sigma$ upper limits, as determined from IMSTAT, in units of mJy. Uncertainties include both statistical and systematic error terms. The systematic error is estimated from the ratio of the measured calibrator fluxes over its estimated historical value based on monitored light curves (typical variance was 5–20 per cent).

historical values from calibration monitoring efforts.[3] Importantly, aside from one case at day ∼400, and in spite of sometimes strong intrinsic variability and scintillation effects, the phase calibrators never strayed more than ≈20 per cent from their nominal historical values, as shown in Fig. 1. Both source and calibration data were inspected with the aim to flag and remove bad time intervals and channels, time intervals strongly affected by interference, and obvious emission and absorption lines. The calibration tables were applied to the Circinus Galaxy data, from which deconvolved, primary-beam-corrected images were made. Due to the increasing beam size of ATCA with decreasing frequency, we measured flux densities using only the 6 km baselines for frequencies below 4 GHz in order to limit contamination to SN 1996cr from the diffuse emission of the host galaxy. Phase self-calibration was employed when feasible, and only if it led to a substantial improvement in the rms noise. Point source flux densities (determined from IMFIT or UVFIT) or $3\sigma$ upper limits (determined from IMSTAT) were then determined for SN 1996cr. These values are provided in Table 1 and shown in Fig. 1. The larger errors on the 15–90 GHz data points reflect greater uncertainties in atmospheric corrections and flux calibrators. Some of the dispersion among the 15–25 GHz points could also arise from contamination by weak $H_2O$ maser emission that was not flagged from the continuum (e.g. Greenhill et al. 1997; McCallum, Ellingsen & Lovell 2007).

The only other strong point source in the field of view is the nucleus of the Circinus Galaxy, which is primarily due to emission from the Compton-thick active galactic nucleus (AGN) as well as a compact circumnuclear starburst. Flux measurements from the point-like nucleus were extracted in a manner identical to SN 1996cr. These are shown in Fig. 1 and provided in the Appendix. While the nucleus could vary intrinsically and can additionally be contaminated at long wavelengths by diffuse emission from the extended disc, it at least provides us with a secondary estimate of any systematic error associated with each observation. We find that the majority of measurements of the nucleus lie between 10 and 30 per cent of its mean total flux in each band, although some observations vary upwards considerably. For instance, at 22.5 GHz there may be possible contamination from water maser emission and varies by a factor of up to 4, while at low frequencies the host galaxy contaminates as a function of the beamsize and varies by factors as large as ∼10–50. Thus, aside from our previously stated reservations regarding the 15–90 GHz data, we are generally confident in our calibrated fluxes for SN 1996cr.

SN 1996cr was observed on 2009 January 25 with the Molonglo Observatory Synthesis Telescope (MOST) at 843 MHz with a synthesized beam of 47 arcsec × 43 arcsec at a position angle of 0°. The MOST data were reduced and calibrated using a custom process described in Bock, Large & Sadler (1999). Given the 24 arcsec north–south separation of SN 1996cr from the bright nucleus of the Circinus Galaxy, the SN emission was completely blended with that of the galaxy. Fortunately, there were three prior MOST observations of this field with SN 1996cr absent or self-absorbed: 1989 April, 1996 April and 1997 April. Difference images were formed after regridding all images to a common reference frame (see Fig. 2). A point source fit to each difference image yielded a mean flux density for SN 1996cr of $520 \pm 30$ mJy and a position fully consistent with the *Chandra* position. Note that the total flux density for the Circinus Galaxy in 1996 was $\sim 2.15 \pm 0.15$ Jy at 843 MHz. Since the flux contribution from the AGN is expected

[3] http://www.narrabri.atnf.csiro.au/calibrators/

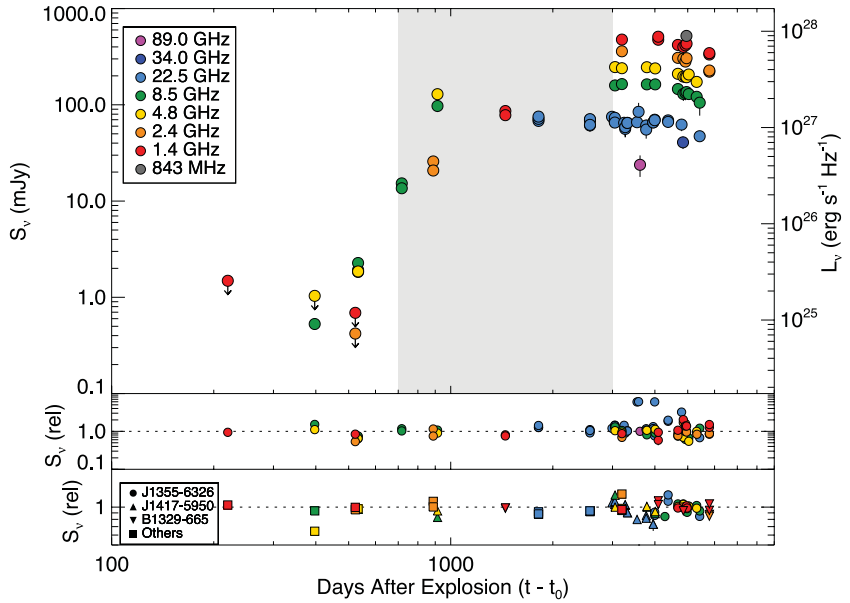


**Figure 1.** Observed radio flux densities (filled circles) for SN 1996cr along with 1$\sigma$ error bars (which are smaller than symbols in some cases); when no secure detection is obtained we show 3$\sigma$ upper limits (e.g. at early times). The grey-shaded region denotes the period between days ∼700–3000 when the shock is believed to be travelling through the dense shell. Three regions are clearly defined, with low early emission (for which only upper limits are available), a flux rise at ∼700 d when the shock begins to interact with the shell, and a late-time plateau region with a possible turnover at day ∼5000. Also shown are the relative flux densities for the host AGN nucleus (middle panel) and various phase flux calibrators (lower panel). The nucleus values were normalized based on the average values at each frequency found in the highest resolution configurations only (e.g. 6A), while the calibrators were normalized based on their historical values at each frequency. In general, the nucleus only varies by ≈10–30 per cent, while the calibrators vary by ≈10–20 per cent. These should provide strict empirical upper limits to any uncertainties on SN 1996cr's variability.

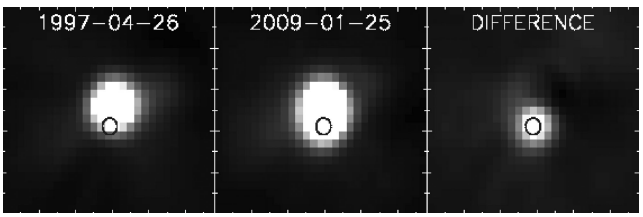


**Figure 2.** We show two 843 MHz images from MOST for the central 4.5 arcmin × 4.5 arcmin of the Circinus Galaxy before (left-hand panel) and after (middle panel) SN 1996cr became visible at 843 MHz, as well as a difference image with the clear SN 1996cr detection (right-hand panel). A 10 arcsec radius black circle denotes the position of SN 1996cr in all panels for reference. All of the images are scaled linearly on an identical stretch from S$_\nu$=0.05–1 Jy. The sidelobes in the images come from the central gap in the array and do not fully subtract out due to radio interference.

to be minimal (roughly 75 mJy with only 10–30 per cent variability), the observed flux must arise almost exclusively from diffuse component and hence should not vary.

## 3 MODELLING THE LIGHT CURVE

### 3.1 Radio emission

The interaction between the SN ejecta and the CSM results in the formation of a double-shocked structure separated by a contact discontinuity. Charged particles are accelerated to relativistic energies across the shock front, giving rise to non-thermal synchrotron emission in the presence of a strong magnetic field. Electrons, being substantially less massive, are easier to accelerate (in the direction perpendicular to their motion) by the magnetic field, and end up dominating the emission. Their energy distribution is assumed to be a power law of the form $N(E) = KE^{-\gamma}$, where $E$ is the electron energy, $K$ is the normalization of the distribution and $\gamma$ is the electron spectral index. Following the prescription given in Chevalier (1982), the synchrotron luminosity $L_\nu$ at frequency $\nu$ is

$$L_\nu = 4\pi R^2 \Delta R\, K\, B^{\alpha+1}\, \nu^{-\alpha}\, \mathrm{e}^{-\tau}\ (\mathrm{erg\,s^{-1}\,Hz^{-1}}), \quad (1)$$

where $\Delta R$ is the thickness of the synchrotron-emitting region at radius $R$, assumed in this case to be the spherically symmetric region encompassing the forward and reverse shocks, $B$ is the magnetic field strength, the radio spectral index is $\alpha = (\gamma - 1)/2$ and $\tau$ is the optical depth.

Radio emission can be absorbed either by synchrotron self-absorption (SSA) or free–free absorption (FFA) from CSM both inside (attenuating backside emission) and outside (attenuating all emission) of the forward shock, leading to telltale low-frequency absorption. We initially assume that all of the absorption is due to FFA (see Section 3.2 for reasoning) and use the form of the FFA optical depth given in Altenhoff et al. (1960):

$$\tau_{\mathrm{ff}} = 8.235 \times 10^{-2}\, \nu_{\mathrm{GHz}}^{-2.1} \int_0^{s_{\mathrm{pc}}} N_{\mathrm{e_{cm^{-3}}}}^2\, T_{\mathrm{K}}^{-1.35}\, \mathrm{d}s_{\mathrm{pc}}, \quad (2)$$

where $T$ is the temperature of the CSM, $\nu$ is the frequency and $N_{\mathrm{e}}$ is the line-of-sight electron number density. Early absorption can be high due to the strong density gradient in the stellar wind, which should decrease as the shock wave overtakes more of the CSM, resulting in a rapid frequency-dependent turn-on like that observed in the spectra of SN 1996cr in Fig. 3.

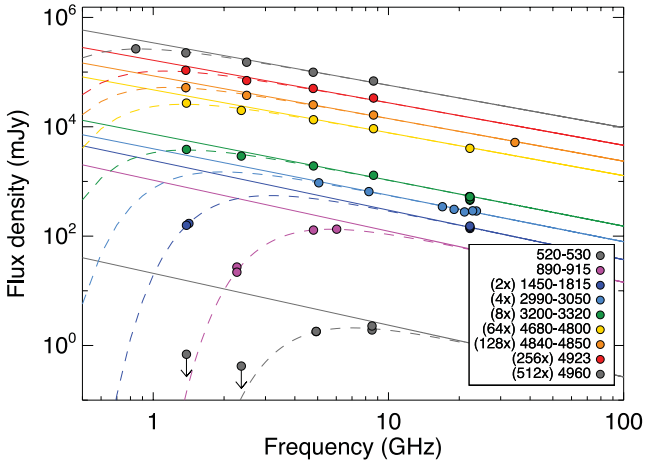


**Figure 3.** Radio spectra of SN 1996cr for selected epochs indicated in the legend as days after explosion. Flux densities (filled circles) are shown with $1\sigma$ error bars (which are smaller than symbols in some cases) or $3\sigma$ upper limits (downward arrows). The intrinsic and absorbed spectra are represented by solid and dashed lines, respectively, with the latest spectra at the top. For clarity, fluxes are plotted with the multiplicative factors in parenthesis. Early-time spectra show high absorption, mostly affecting the lower frequencies as expected from FFA. The effect of adopting a varying spectral index (see Section 3.2 and Fig. 4) can be seen in the intrinsic models plotted at each epoch.

### 3.2 Empirical radio properties

A key constraint on the nature of the radio emission is its spectral index. Measuring this for SN 1996cr, however, is non-trivial, since this object was largely observed via serendipitous observations with sparse frequency coverage, while additionally the data during the first 1000 d appear to be heavily absorbed (Fig. 3). In order to deal with the lack of multifrequency observations at each epoch, the available data were grouped together in periods of up to six months where possible, during which the spectral index is assumed to remain constant to within our measurement errors.

A constant spectral index is generally assumed for RSNe, but the data for SN 1996cr allow us to confront this assumption directly. We note that the late-time data for SN 1996cr, between days ∼2800 and 5000, exhibit minimal absorption, and thus provide relatively strong constraints on the intrinsic spectral index. For epochs with wide frequency coverage, an FFA optical depth and spectral index were computed using the Levenberg–Marquart least-squares method. Limits on the optical depth for epochs with poor low-frequency coverage were set equal to the value from the last well-fitted spectrum. These limits are of minimal consequence, as the free-fit spectral indices in epochs where such optical depth limits exist only show marginal variations to changes in the limiting optical depth values. The constraints on the optical depths and the values of the spectral indices are listed in Table 2.

As seen in Fig. 4, well-constrained values of the intrinsic spectral index between days ∼3000 and 5000 appear to shift to flatter values at later times, and a weighted linear regression fit (OLS Y|X; Isobe et al. 1990) to the values of the spectral index shows evidence for mild spectral flattening (nominally $\sim 10\sigma$ confidence), which we assume to be the intrinsic variation of the spectral index. A constant $\alpha$ model, however, cannot be ruled out using $\chi^2$ or likelihood ratio statistics (only $\sim 1.5\sigma$ confidence), leaving doubts about the veracity of the trend. Extrapolation of this trend back to days ∼520, ∼900 and ∼1600–1900 is consistent with the data, although these values are not well constrained due to stronger degeneracies between their spectral indices and absorption.

We characterize the evolution of the intrinsic spectral index of SN 1996cr in a manner similar to that used for SN 1987A in Zanardo et al. (2010). The intrinsic spectral index is given by $\alpha(t) = \alpha_0 + \beta_0 \times (t - t_0)/\Delta$, where $t$ is given in days, $t_0 = 3000$ d, $\Delta = 365.25$ d, $\alpha_0 = 0.852 \pm 0.002$ and $\beta_0 = -0.014 \pm 0.001$. Errors on regression parameters were assessed through jackknife resampling. We extrapolate this regression back to day 400 (see Fig. 4) and rely on the fixed values of the spectral index from the above fit to reassess values of the optical depth that will be used in the subsequent analysis. The specific (fixed) values of the spectral index and the refitted values of the optical depth are also listed in Table 2.

**Table 2.** Selected epochs with corresponding free-fit optical depth and spectral index, final optical depth and fixed spectral index.

| Days since explosion | $\tau_0$ ($K^{-1.35}$ pc $cm^{-6}$) (free-fit) | Spectral index (free-fit) | $\tau_0$ ($K^{-1.35}$ pc $cm^{-6}$) (refitted) | Spectral index (fixed) |
|---|---|---|---|---|
| 397 | 30.00 † | 1.00 † | 30.00 † | 0.95 |
| 530* | 28.16 ± 2.56 | 1.00 † | 27.07 ± 2.54 | 0.95 |
| 897* | 16.67 ± 4.97 | 0.87 ± 0.86 | 17.05 ± 0.51 | 0.93 |
| 1607* | 3.75 ± 2.11 | 0.71 ± 0.38 | 4.82 ± 0.16 | 0.91 |
| 3039* | 1.87 ± 5.20 | 0.86 ± 0.13 | 1.66 ± 1.60 | 0.85 |
| 3270* | 0.72 ± 0.23 | 0.83 ± 0.05 | 0.78 ± 0.13 | 0.84 |
| 3676 | 0.70 † | 0.83 ± 0.04 | 0.70 † | 0.83 |
| 4013 | 0.73 ± 0.18 | 0.84 ± 0.05 | 0.64 ± 0.06 | 0.81 |
| 4737* | 0.39 ± 0.34 | 0.70 ± 0.08 | 0.70 ± 0.19 | 0.79 |
| 4849* | 0.58 ± 0.58 | 0.80 ± 0.09 | 0.51 ± 0.40 | 0.78 |
| 4923* | 0.15 † | 0.64 ± 0.12 | 0.46 ± 0.41 | 0.78 |
| 4959* | 0.13 ± 0.15 | 0.67 ± 0.11 | 0.27 ± 0.06 | 0.78 |
| 5035 | 0.10 † | 0.83 ± 0.20 | 0.10 † | 0.77 |
| 5370 | 0.10 † | 0.84 ± 0.09 | 0.10 † | 0.76 |

*Note.* Only epochs marked with an asterisk are used in the subsequent analysis, as they provide the most reliable constraints on the refitted optical depth. Values marked with † denote instances where the parameter pegged at the reasonable imposed upper or lower limits that we set in the fitting routine; the corresponding parameter ($\tau_0$ or spectral index $\alpha$) was therefore evaluated at this fixed value and its errors should be regarded with caution.

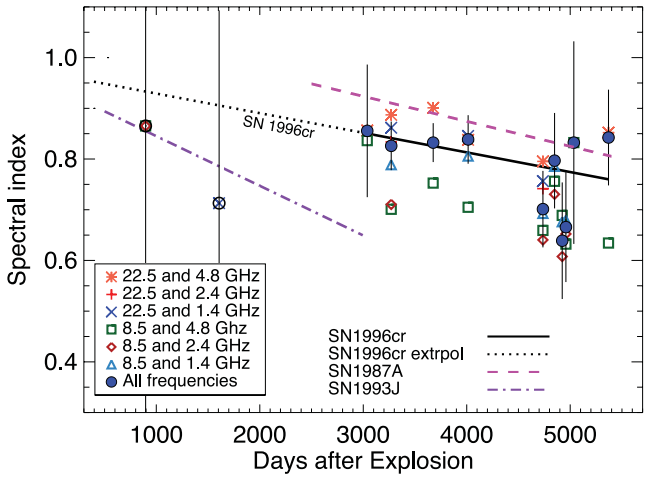


**Figure 4.** Points show the intrinsic spectral indices and $1\sigma$ errors derived from linear regression fits to the SN 1996cr spectra shown in Fig. 3. Also shown are all available two frequency spectral indices for a given epoch (errors are not shown for plot clarity, but can be assessed using Table 1). A linear regression fit to the well-constrained spectral indices from days 3000–5000 versus time suggests that the spectral slope may be flattening, similar to the spectral index variations seen in both SN 1987A and SN 1993J (see the text for details), although the result is not yet robust. Early best-fitting spectral indices for SN 1996cr are not included in this parametrization, but are consistent with our extrapolation of the best-fitting time evolution to within their large errors.

The mild evolution of the spectral index of SN 1996cr is similar to that of the highly monitored SN 1987A (Zanardo et al. 2010). Fig. 4 also shows the spectral index variation for SN 1993J; we note that Weiler et al. (2007) assumed a constant spectral index for this SN, but its spectral index clearly appears to vary based on fig. 4 of Weiler et al. (2007), fig. 7 of Chandra, Ray & Bhatnagar (2004) and fig. 8 of Martí-Vidal et al. (2011). From the data in the ∼80–3000 d period from Weiler et al. (2007), a constant spectral model is rejected at a 100 per cent confidence level. We characterize a varying spectral model for SN 1993J as $\alpha = 0.865 \pm 0.003$ at day 800, and a decay rate of $\Delta\alpha = -0.036 \pm 0.001$ yr$^{-1}$.

It is intriguing that the spectral indices of arguably the three best-studied RSNe all show evidence for spectral flattening with time. This variation runs counter to some theoretical predictions (e.g. Ellison, Decourchelle & Ballet 2004; Berezhko & Ksenofontov 2006; Tatischeff 2009) and clearly warrants further investigation. It is still unclear whether this spectral flattening is a ubiquitous property of young RSNe. For instance, SN 1979C also has a considerable amount of radio data available and appears to remain constant since day 2000 (see fig. 3 of Montes et al. 2000), although difficulties associated with disentangling spectral and CSM variations and the large scatter in measured spectral indices could easily mask subtle spectral changes such as those observed in Fig. 4. SN 1986J, on the other hand, shows strong, complex spectral variations with time. Very long baseline interferometry (VLBI) observations suggest that these variations appear to stem from the flat spectrum of the remnant core brightening as the steep spectrum of the shell fades (Bietenholz, Bartel & Rupen 2010). Thus, neither SN 1979C nor SN 1986J provide 'clean' examples. Other RSNe, such as SN 1980K and SN 1994I show hints of spectral variations, while SN 1978K, SN 1995N and SN2001ig remain thoroughly ambiguous (Montes et al. 1998; Ryder et al. 2004; Smith et al. 2007; Chandra et al. 2009; Weiler et al. 2011); unfortunately, all are relatively weak radio sources and hence too poorly constrained to provide compelling examples either for or against spectral flattening. Clearly interpreting mild evolutionary trends (e.g. SN 1993J) should be done with caution, given the obvious degeneracies between parameters responsible for the synchrotron spectrum in SNe. Past and future LBA imaging can marginally resolve SN 1996cr and could highlight any strong spectral variations in this source (Bartel et al., in preparation).

The brightness temperature of SN 1996cr, which is calculated from the simulated shock expansion and the FFA-corrected data, does not exceed the value of $\approx$2–4 $\times$ $10^{11}$ K (there is a very weak frequency dependence) which typically leads to SSA (Readhead 1994). However, this limit may be reached for hypothetical low frequency data points around day 800, which suggests a possible combination of FFA and SSA at early times, although this is not well constrained with our limited data. We model this in more detail in the next section.

### 3.3 Hydrodynamical simulation

We based our work on the one-dimensional hydrodynamical simulations by Dwarkadas et al. (2010) which provide the hydrodynamic and kinetic information of the ejecta–CSM interaction. Without detailed calculations and an examination of the microscopic physics, which is beyond the scope of this paper, it is impossible to calculate the behaviour of the magnetic field and the acceleration of particles to relativistic energies that dictate the strength of the synchrotron emission. One must therefore appeal to simpler scaling relations to infer the behaviour of these quantities in terms of others that are well understood. Chevalier (1996) has outlined several possibilities for how the synchrotron luminosity parameters might scale, although many other variations may exist. The radiating electron energy density ($\propto K$) and the magnetic energy density ($\propto B^2$) may scale with the thermal energy density ($\propto P$), since these are thought to be built up by high-pressure turbulent motions in the shock, or may also scale with the thermal particle density if a constant fraction of the thermal particle density is injected in the acceleration process. Another possibility is that the magnetic energy density may decrease as the surface area ($B^2 \propto r^{-2}$), as the magnetic field is carried out from the surface of the progenitor via the wind. These simple physical scalings, however, may not provide a complete picture of the likely complex physics involved, as evidenced by the spectral index flattening and the decoupling of the X-ray and radio light curves in SN 1987A, for instance. Although there is a physical basis for the possible energy density scalings, the only SN in which such scaling relations have been successfully constrained (albeit somewhat controversially) is SN 1993J (e.g. Fransson & Björnsson 1998; see also Mioduszewski et al. 2001 for alternative viewpoint), where the magnetic energy density was derived independently from SSA through very early monitoring, and radius constraints were provided by VLBI data (e.g. Marcaide et al. 1997; Bartel et al. 2000); thus, removing several of the degeneracies that force the need for the scaling relations in the first place. We discuss the results of applying a few particular scaling models in Section 4.2.

As mentioned in the previous section, SSA should play a role in the spectral appearance of SN 1996cr at very early times. To incorporate SSA into our radio models in a self-consistent way, we first determined the unabsorbed brightness temperature for each frequency of our radio model versus time, assuming a spherical shell morphology that evolves with the shock radius. We then applied SSA to the full radio model assuming $\tau_{\rm SSA} \sim 1$ at the critical frequency where the brightness temperature surpassed $\approx 3 \times 10^{11}$ K (Readhead 1994). Therefore, the radio model is absorbed by

this model-dependent SSA, in addition to FFA whose constraints on $\tau_{\rm ff}$ are presented in Table 2.

## 4 RESULTS

We initially characterize the ionized region surrounding SN 1996cr and compare the radio constraints on the CSM free electron density to the expectations from hydrodynamic simulation. The simulated radio light curves are then presented for a few basic scaling models, and are evaluated by comparing their individual features to those of the observed light curves. These results set the scope for further research on this object.

### 4.1 Empirical constraints on the CSM

The constraints on the FFA optical depth allow for the study of the CSM ionization by providing limits on the density of free electrons. This in turn can be used as a relatively direct cross-check on the simulation density distribution, since the free electron density provides a strong lower limit on the total mass in the CSM assuming full ionization. For simplicity, we considered a CSM composition of H only, and adopted a scaling factor of 20 (based on the X-ray derived abundances and resulting mean molecular weight of the CSM) to scale our results to the CSM composition of H, He and metals presented for SN 1996cr in Dwarkadas et al. (2010).

Each observation epoch has an approximately corresponding time step in the simulation, and a shock radius is assigned to it based on the position of the forward shock at that time. The free electron density in front of the shock can be determined from the difference in the values of the optical depth between two radio epochs (equation 2). This requires setting a value $N_{\rm e}$ for the outermost shock radius (latest radio epoch) from which to iterate back through the CSM to the innermost shock radius (earliest radio epoch), which we assumed to be $N_{\rm e} = 10^4$ cm$^{-3}$, corresponding to an average value found in H II regions. We adopt this value since SN 1996cr appears to reside at the centre of a diffuse H$\alpha$ clump 5–10 pc in diameter (cf. figs 3 and 5 of Bauer et al. 2008), which is presumably a large extended H II region ionized by several massive stars. For simplicity, we assumed that the CSM has a uniform temperature, and investigated a range of initial CSM temperatures between $T = 10^4$ and $10^6$ K, since these were not directly constrained by the hydrodynamical simulation. This range should be appropriate for a wide range of RSG wind densities (e.g. Fransson & Björnsson 1998 and references therein). Such temperature variations will lead to proportionally higher ionization fractions, although the radial form appears to remain relatively steady. The shock radii and constraints on $N_{\rm e}$ are listed in Table 3 for $T = 10^4$ K. The number densities of total electrons that are available to be ionized are obtained from the simulation over the same CSM regions delimited by the radio epochs. Finally, the CSM ionization fraction is calculated directly from the free and total electron densities, and is shown in Fig. 5.

**Table 3.** Selected epochs with corresponding shock radii and constraints on $N_{\rm e}$, determined from the hydrodynamic simulation and constraints on the FFA optical depth.

| Days since explosion | Radius ($10^{17}$ cm) | $N_{\rm e}$ ($10^4$ cm$^{-3}$) |
|---|---|---|
| 530 | 0.918 | $(2.59 \pm 0.16)$ |
| 897 | 1.058 | $(2.14 \pm 0.14)$ |
| 1607 | 1.256 | $(1.32 \pm 0.23)$ |
| 3039 | 1.825 | $(1.06 \pm 0.26)$ |
| 3270 | 1.921 | $(0.94 \pm 0.14)$ |
| 4737 | 2.620 | $(1.05 \pm 0.16)$ |
| 4849 | 2.667 | $(1.03 \pm 0.14)$ |
| 4923 | 2.717 | $(1.03 \pm 0.08)$ |
| 4959 | 2.766 | 1.00 |

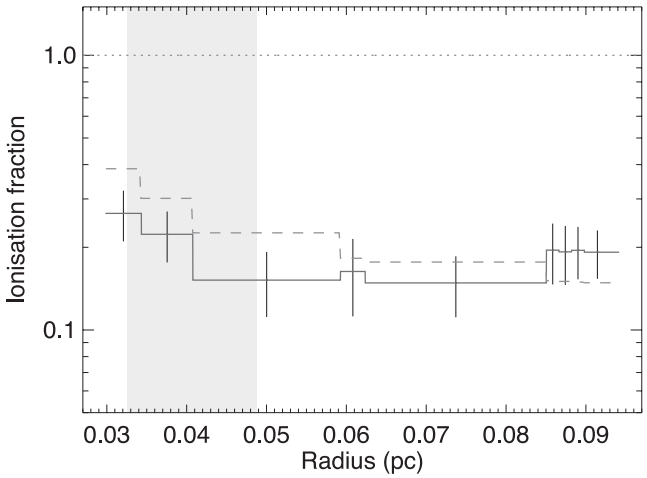


**Figure 5.** The CSM ionization fraction and $1\sigma$ error computed from constraints on the FFA optical depth (solid line), and the theoretical ionization fraction for comparison (dashed line), for a CSM temperature of $10^4$ K. The presumed location of the dense shell is denoted by the grey-shaded region.

The radio-constrained free electron densities appear fully in line with (i.e. lower than) the total electron densities from the hydrodynamical simulation for temperatures lower than $10^5$ K. Overall, the CSM ionization fraction decreases slightly with radius; this is fully consistent with our expectations, based on recombination after a strong flash ionization from the SN outburst ionizing our adopted CSM density distribution. We are relatively confident in our adopted value of $N_{\rm e}$ for the latest radio epoch, as all values lower than $5 \times 10^4$ cm$^{-3}$ appear stable, yielding ionization fractions that are consistent with the simulation, while values over this tend to drive the ionization in all shells to significantly higher ionization fractions.

As an additional check, we obtain the CSM neutral fraction directly from the ionized fraction, and use it to calculate the neutral hydrogen column, which we then compare to the one obtained from spectral fits to the X-ray data. Between 1999 June (∼1450 d) and 2009 January (∼5000 d), the CSM neutral fraction implies a neutral hydrogen column density of $N_{\rm H} = (9.3 \pm 2.2) \times 10^{20}$ amu cm$^{-2}$, which is roughly consistent with a physical measurement of $N_{\rm H} = 1.8 \times 10^{21}$ amu cm$^{-2}$ presented in Dwarkadas et al. (2010), based on differential spectral fits to the 2000 and 2009 Chanda High Energy Transmission Grating (HETG) data. Although there may be a slight difference in the regions being considered for both these column densities, it is perhaps more likely that these values differ as a result of the latter being constrained by model fits to the X-ray spectrum, which can be easily affected by low-energy spectral lines.

We can also crudely estimate the evolution of the CSM ionization following shock breakout on theoretical grounds to obtain an interesting consistency check with the hydrodynamic simulation. An SN explosion with an average output energy of $\sim 10^{51}$ erg will radiate $(0.5–2.3) \times 10^{57}$ ionizing photons during the first 1.5 d (Ensman & Burrows 1992), which at the higher end is sufficient to ionize up to $\sim 2$ M$_\odot$ of material (Lundqvist & Fransson 1996), assuming the CSM is pure H. The CSM mass in the hydrodynamic simulation is about 2.1 M$_\odot$, and thus could possibly be almost completely ionized by the shock breakout. We therefore assume that the entire model CSM is initially ionized, which provides an upper bound on the true ionization of the CSM; the true CSM is likely to be less

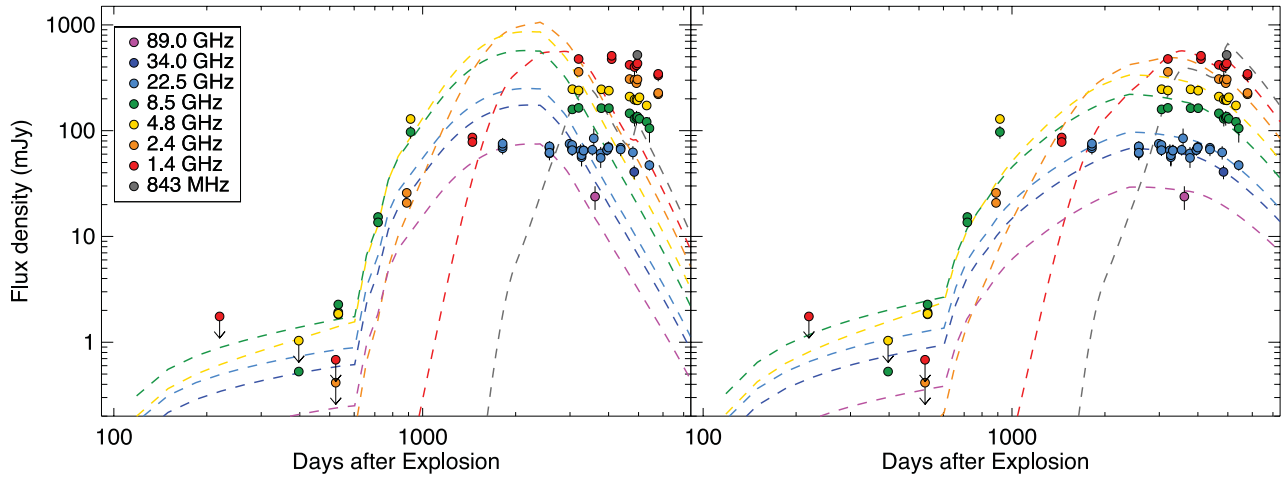


**Figure 6.** Simulated light curves (lines) and observed radio flux densities (circles) for SN 1996cr. Left: the 'standard' model scales $K$ and $B^2$ as the thermal energy density (erg cm$^{-3}$). We fixed the constants of proportionality for the $K$ and $B^2$ scalings at a radius of $10^{16}$ cm to be $\approx 3.4 \times 10^{-5}$ and $\approx 1.3$, respectively, so as to best fit the data. This model provides an intrinsic flux rise at $\sim$700 d but fails to match the late-time plateau region. Right: $K$ scales as the thermal particle density (cm$^{-3}$) and $B^2$ scales as the surface area (cm$^{-2}$). The constants of proportionality for $K$ and $B^2$ at a radius of $10^{16}$ cm are fixed to $\approx 4.2 \times 10^{17}$ and $\sim 10^{26}$, respectively. Although the simulated light curve provide a better match to the late-time data, the flux at day $\sim$900 is nearly of an order of magnitude lower than observations.

ionized if it is not distributed in a spherically symmetric manner, has a mass significantly higher than 2 $M_\odot$ or the explosion energy is lower. We model the recombination using the initial CSM density distribution from the hydrodynamical simulation (for which we assume a CSM composition of pure H, and scale to a composition of H, He and metals with our assumed scaling factor) and the H II recombination rates given in Seager, Sasselov & Scott (2000, i.e. $\alpha_B = 2.6 \times 10^{-13}$ cm$^3$ s$^{-1}$ for our assumed CSM temperature). As two examples, we note that the CSM densities of free electrons at 0.04 pc (within the shell) and 0.12 pc (within the assumed RSG wind) are $1.5 \times 10^6$ and $6 \times 10^4$ cm$^{-3}$, and will completely recombine in 0.08 and 2.1 yr, respectively.

The X-ray radiation from the SN shock provides an ongoing source of energy for reionization of recently recombined material. To model the amount of ionizing photons that the shock injects into the CSM as a function of time, we assume that the ionizing photon rate scales linearly with the X-ray light curve. Using the same absorbed non-equilibrium ionization model adopted in Dwarkadas et al. (2010), we normalized the photon rate to $2.7 \times 10^{48}$ photons s$^{-1}$ on day $\sim$1670 to match the absorbed photon rate from the 2001 August *XMM* spectrum. Our simulation shows that as the shock moves through the CSM, it largely reionizes the immediate region around it (i.e. the bin it is in), but nothing more. Thus, the vast majority of the line-of-sight ionization we observe comes from the initial shock-breakout ionization. The resulting CSM ionization fraction is shown for comparison in Fig. 5. From this model, the theoretical neutral column density in the 1450–5000 d period is $N_{\rm H} = (9.4 \pm 1.9) \times 10^{20}$ amu cm$^{-2}$, in accord with the value from the HETG 2000–2009 data.

### 4.2 Simulation of the radio light curve

As a test of our methods, we initially computed radio light curves for a hydrodynamic simulation of a self-similar shock expansion to demonstrate that we could correctly reproduce the decline rates of the synchrotron luminosity presented in Chevalier (1996) for the different models therein. We then applied this code to the more complex simulation of Dwarkadas et al. (2010), scaling the simulated light curves to the radio data.

For SN 1996cr there are three conditions that the observations require if the model is to successfully simulate the light curve. (1) Low emission while the ejecta is moving within the sparse cavity, since we have upper limits for this from both X-rays and radio. (2) A sharp increase in flux from $\sim$700 to $\sim$1000 d, as the SN ejecta initially impacts and interacts with the dense shell. The fluxes in the 4.8 and 8.5 GHz bands rise together, which indicates that the rise is intrinsic rather than the result of diminishing absorption, since FFA (or SSA for that matter) will affect the bands differently. (3) A flattening of the light curve between days $\sim$1000 and $\sim$4000, with the beginning of a decrease/turnover at very late times.

Fig. 6 shows the simulated radio light curves for two different models. The standard model in Chevalier (1996), relating $K$ and $B^2$ to the thermal energy density, proved inadequate in our simulations. It provides a fair match to the luminosity rise around day 700, but the subsequent peak in luminosity decreases too quickly as the forward shock leaves the shell. The second model, which relates $K$ to the thermal particle density and $B^2$ to the surface area, does a better job at fitting the late-time data, but fails however to fit the data from the rise, since the simulated flux around day 900 is almost one order of magnitude lower than the observations. In our model, we have assumed that the radio emission is generated from both the forward and reverse shocks, as the forward shock-only light curve resulted in poor fits to the data (i.e. lack of plateau region followed by a sharp falloff).

More complex scalings may allow us to potentially fit the entire radio light curve, but remain ad hoc due to our currently poor understanding of the detailed microphysics that ultimately drives the large-scale radio emission. This obviously makes it difficult to assess whether the deviations between radio data and models stem from our simplistic approach, which assumes that the emission at all times and all locations arises from both shocks, or alternatively, may still be limited by the hydrodynamic simulation. While the simulation has some difficulty reproducing a similar feature in the X-ray light curve (Dwarkadas et al. 2010), it is able to reproduce the X-ray spectra and light curves, which are more directly and

fundamentally tied to physical parameters (e.g. density, emissivity and ionization equilibrium), and even allow to separate X-ray emission from the forward shock, which dominates during the first seven years, and reverse shock, which dominates thereafter. Our radio calculations, on the other hand, do not allow this level of accuracy or differentiation.

## 5 DISCUSSION AND CONCLUSIONS

We have presented an up-to-date sequence of radio light curves of SN 1996cr. Using an analytic model that describes the radio emission from SNe, combined with a hydrodynamic simulation of the synchrotron-emitting regions, we simulated the observed radio light curves of SN 1996cr to further constrain the density of the CSM, particularly in the sparse region interior to the shell, for which there are no firm X-ray constraints implemented in the hydrodynamic simulation.

To this end, we explored some basic scalings that relate the hydrodynamics of the shock to the magnetic field and the radiating electron distribution that are required for synchrotron emission. For all of the models studied, we found that the behaviour in certain periods of our simulated radio light curves matched the functional form of our observations relatively well, but invariably failed to match the most tightly constraining temporal features, typically the rise around $\sim$700 d and/or the plateau region between $\sim$2000 and 5000 d.

The simulation shown on the right-hand panel in Fig. 6 (with $K \propto$ thermal particle density and $B^2 \propto$ surface area) matches the radio light curves reasonably well from a radius of $\approx$0.04 pc outwards. The different scalings that we studied have their share of assumptions and potential failings. However, the mismatch interior to $\approx$0.04 pc coincides with the lack of strong constraints on the simulation parameters from the X-ray light curve at similar radii, which may mean that the inner region of the dense shell is not being adequately modelled. To improve the early discrepancies, we need to understand how the magnetic field and accelerated particle distribution actually scale as the SNe shock collides with a dense CSM shell, and/or have the simulation potentially consider (1) a more concentrated shell mass along the inner edge, (2) clumpy structure that could provide modifications to both the ionization and radio flux, (3) asymmetric mass distribution to spread out/flatten the peak, or (4) modification to the SN parameters (e.g. ejecta density slope, the ejecta mass and explosion energy). Changes to the simulations, however, cannot be too large, since the non-equilibrium ionization model spectra already match the HETG X-ray spectra well over several epochs.

Geometrical considerations, such as possible asymmetries in the wind, in the SN explosion or in the dense shell, were not included in our calculations. Dewey, Bauer & Dwarkadas (2011) recently showed that SN 1996cr might in fact not be spherically symmetric. Nevertheless, our assumption that a one-dimensional hydrodynamic simulation is appropriate to simulate the radio light curve is at least justified by the fact that it also reproduces the broad features of the observed X-ray light curve (Dwarkadas et al. 2010).

Of course, the X-ray emission is thermal, while the radio emission is non-thermal synchrotron. These are very different mechanisms, arising from potentially distinct regions and scaling with different physical parameters; the microphysics and mechanics of which are poorly understood or constrained in the radio. Thus, we should not be surprised to see a decoupling of the simulated X-ray and radio light curves. Clearly, the physics that generates the X-ray emission is much simpler than that of the radio, as it relates only to the density, emissivity and ionization (in)equilibrium of the emitting material. This close link between the hydrodynamical parameters of the shock and a correct simulation of the observed X-ray light curve lends more support to the hydrodynamic simulation as accurately descriptive of the dynamics of the shock. We attempted to simulate the radio light curve using simple assumptions for the magnetic field and the electron distribution, which do not appear to be appropriate for complex objects such as SN 1996cr. The use of simple scaling relations, combined with hydrodynamic simulations, also failed to adequately reproduce the sharp rise and subsequent linear increase of radio emission in SN 1987A (Dwarkadas 2007b,c). These are precautions to be considered when trying to constrain the circumstellar density of these objects using simple radio models, because even if an X-ray-based density model is available, it may not be able to accurately model the radio light curve while avoiding the degeneracies that arise in trying to determine viable density scalings.

SN 1996cr remains quite bright at nearly all wavelengths, and future radio and X-ray monitoring will be able to constrain the apparent decline, which should place stronger constraints on the outer wind and CSM density distribution. Future monitoring with the LBA and Atacama Large Millimeter/submillimeter Array (ALMA) will be able to resolve the radio morphology of SN 1996cr in greater detail to constrain its spatial expansion (i.e. current velocity) and emission regions.

## ACKNOWLEDGEMENTS

CM and FEB would like to thank Andrés Jordán for suggestions. Special thanks to Juergen Ott for providing the 89 GHz reduced data and Shari Breen for early access to her data. We acknowledge support from CONICYT-Chile under grants FONDECYT 1101024 (CM, FEB), ALMA-CONICYT 31100004 (FEB), and FONDAP-CATA 15010003 (FEB), Basal-CATA grant PFB-06/2007 (FEB), the Iniciativa Científica Milenio through the Millennium Center for Supernova Science grant P10-064-F with input from 'Fondo de Innovación para la Competitividad, del Ministerio de Economía, Fomento y Turismo de Chile' (FEB), and Chandra X-ray Center grants SAO GO9-0086, GO0-11095 and GO1-12095B (FEB, VVD).

FEB thanks the ATNF Distinguished Visitor programme. The ATCA is part of the Australia Telescope National Facility which is funded by the Commonwealth of Australia for operation as a National Facility managed by CSIRO. This paper includes archived data obtained through the Australia Telescope Online Archive (http://atoa.atnf.csiro.au). The MOST is operated by the University of Sydney with support from the Australian Research Council.

## REFERENCES

Altenhoff W., Mezger P. G., Wendker H., Westerhout G., 1960, Veröff. Sternwärte, Bonn, 59, 48

Bartel N. et al., 2000, Sci, 287, 112

Bauer F. E., Smartt S., Immler S., Brandt W. N., Weiler K. W., 2007, in Immler S., Weiler K. W., McCray R., eds, AIP Conf. Proc. Vol. 937, Supernova 1987A: 20 Years After: Supernovae and Gamma-Ray Bursters. Am. Inst. Phys., New York, p. 427

Bauer F. E., Dwarkadas V. V., Brandt W. N., Immler S., Smartt S., Bartel N., Bietenholz M. F., 2008, ApJ, 688, 1210

Berezhko E. G., Ksenofontov L. T., 2006, ApJ, 650, 59

Bietenholz M. F., Bartel N., Rupen M. P., 2010, ApJ, 712, 1057
Bock D. C.-J., Large M. I., Sadler E. M., 1999, AJ, 117, 1578
Chandra P., Ray A., Bhatnagar S., 2004, ApJ, 612, 974
Chandra P. et al., 2009, ApJ, 690, 1839
Chevalier R. A., 1982, ApJ, 259, 302
Chevalier R. A., 1996, in Taylor A. R., Paredes J. M., eds, ASP Conf. Proc. Vol. 93, Radio Emission from the Stars and the Sun. Am. Inst. Phys., New York, p. 125
Chevalier R. A., Fransson C., 1994, ApJ, 420, 268
Chevalier R. A., Liang E. P., 1989, ApJ, 344, 332
Dewey D., Bauer F. E., Dwarkadas V. V., 2011, in McEnery J. E., Racusin J. L., Gehrels N., eds, AIP Conf. Proc. Vol. 1358, Gamma-Ray Bursts 2010. Am. Inst. Phys., New York, p. 289D
Duffy P., Ball L., Kirk J. G., 1995, ApJ, 447, 364
Dwarkadas V. V., 2005, ApJ, 630, 892
Dwarkadas V. V., 2007a, ApJ, 667, 226
Dwarkadas V. V., 2007b, Rev. Mex. Astron. Astrofis. Conf. Ser., 30, 49
Dwarkadas V. V., 2007c, in Immler S., Weiler K. W., McCray R., eds, AIP Conf. Proc. Vol. 937, Supernova 1987A: 20 Years After: Supernovae and Gamma-Ray Bursters. Am. Inst. Phys., New York, p. 120
Dwarkadas V. V., Dewey D., Bauer F. E., 2010, MNRAS, 407, 812
Ellison D. C., Decourchelle A., Ballet J., 2004, A&A, 413, 189
Elmouttie E., Haynes R. F., Jones K. L., Ehle M., Beck R., Wielebinski R., 1995, MNRAS, 275, L53
Ensman L., Burrows A., 1992, ApJ, 393, 742
Fransson C., Björnsson C., 1998, ApJ, 509, 861
Freeman K. C., Karlsson B., Lynga G., Burrell J. F., van Woerden H., Goss W. M., Mebold U., 1977, A&A, 55, 445
Greenhill L. J., Ellingsen S. P., Norris R. P., Gough R. G., Sinclair M. W., Moran J. M., Mushotzsky R., 1997, ApJ, 474, L103
Isobe T., Feigelson E. D., Akritas M., Babu G. J., 1990, ApJ, 364, 104
Jones K. L., Koribalski B. S., Elmouttie M., Haynes R. F., 1999, MNRAS, 302, 649
Koribalski B. S. et al., 2004, AJ, 128, 16
Lamers H. J. G. L. M., Maeder A., Schmutz W., Cassinelli J. P., 1991, ApJ, 368, 538
Lundqvist P., Fransson C., 1996, ApJ, 464, 924
Marcaide J. M. et al., 1997, ApJ, 486, L31
Martí-Vidal I., Marcaide J. M., Alberdi A., Guirado J. C., Prez-Torres M. A., Ros E., 2011, A&A, 526, A143
McCallum J. N., Ellingsen S. P., Jauncey D. L., Lovell J. E. J., Greenhill L. J., 2005, AJ, 129, 1231
McCallum J. N., Ellingsen S. P., Lovell J. E. J., 2007, MNRAS, 376, 549
McCallum J. N., Ellingsen S. P., Lovell J. E. J., Phillips C. J., Reynolds J. E., 2009, MNRAS, 392, 1339
Mioduszewski A. J., Dwarkadas V. V., Ball L., 2001, ApJ, 562, 869
Montes M. J., Van Dyk S. D., Weiler K. W., Sramek R. A., Panagia N., 1998, ApJ, 506, 874
Montes M. J., Weiler K. W., Van Dyk S. D., Panagia N., Lacey C. K., Sramek R. A., Park R., 2000, ApJ, 532, 1124
Nugis T., Lamers H. J. G. L. M., 2000, A&A, 360, 227
Park S., Zhekov S. A., Burrows D. N., McCray R., 2005, ApJ, 634, L73
Phillips C. J., Norris R. P., Ellingsen S. P., McCulloch P. M., 1998, MNRAS, 300, 1131
Readhead A. C. S., 1994, ApJ, 426, 51
Reynolds S. P., 2008, ARA&A, 46, 89
Ryder S. D., Sadler E. M., Subrahmanyan R., Weiler K. W., Panagia N., Stockdale C. J., 2004, MNRAS, 349, 1093
Seager S., Sasselov D. D., Scott D., 2000, ApJS, 128, 407
Smith I. A., Ryder S. D., Böttcher M., Tingay S. J., Stacy A., Pakull M., Liang E. P., 2007, ApJ, 669, 1130
Soderberg A. M., Chevalier R. A., Kulkarni S. R., Frail D. A., 2006, ApJ, 651, 1005
Stothers R. B., Chin C.-W., 1996, ApJ, 468, 842
Tatischeff V., 2009, A&A, 499, 191
Tenorio-Tagle G., Bodenheimer P., Franco J., Rozyczka M., 1990, MNRAS, 244, 563
Tenorio-Tagle G., Rozyczka M., Franco J., Bodenheimer P., 1991, MNRAS, 251, 318
Vink J. S., Muijres L. E., Anthonisse B., de Koter A., Grfener G., Langer N., 2011, A&A, 531, 132
Weaver R., McCray R., Castor J., Shapiro P., Moore R., 1977, ApJ, 218, 377
Weiler K. W., Panagia N., Montes M. J., Sramek R. A., 2002, ARA&A, 40, 387
Weiler K. W., Williams C. L., Panagia N., Stockdale C. J., Kelley M. T., Sramek R. A., Van Dyk S. D., Marcaide J. M., 2007, ApJ, 671, 1959
Weiler K. W., Panagia N., Stockdale C., Rupen M., Sramek R. A., Williams C. L., 2011, ApJ, 740, 79
Wilson W. E. et al., 2011, MNRAS, 416, 832
Zanardo G. et al., 2010, ApJ, 710, 1515

## APPENDIX A:

Below we provide flux density tables for the calibrators and nucleus measurements (Tables A1 and A2, respectively), which are shown in the lower panels of Fig. 1. These were reduced in the same manner as the flux densities of SN 1996cr, and demonstrate that the variability we see is real. The full tables are available in the online journal.

**Table A1.** Calibrators.

| Obs. date | Obs. ID | Calibrator | *W* band | | *K*$_a$ band | | *K* band | | *X* band | | *C* band | | *S* band | | *L* band | |
|---|---|---|---|---|---|---|---|---|---|---|---|---|---|---|---|---|
| | | | $\nu$ | $S_\nu$ | $\nu$ | $S_\nu$ | $\nu$ | $S_\nu$ | $\nu$ | $S_\nu$ | $\nu$ | $S_\nu$ | $\nu$ | $S_\nu$ | $\nu$ | $S_\nu$ |
| (1) | (2) | (3) | (4) | (5) | (6) | (7) | (8) | (9) | (10) | (11) | (12) | (13) | (14) | (15) | (16) | (17) |
| 1995-03-03 | C204a | 1329-665 | – | – | – | – | – | – | 8640 | 348.0 ± 11.6 | 4800 | 854.0 ± 14.1 | – | – | – | – |
| 1995-03-03 | C204a | 1329-665 | – | – | – | – | – | – | 8640 | 348.0 ± 11.6 | 4800 | 854.0 ± 14.1 | – | – | – | – |
| 1995-03-30 | C363 | 1329-665 | – | – | – | – | – | – | – | – | – | – | – | – | 1418 | 2680.0 ± 34.0 |
| 1995-04-16 | C418 | 1329-665 | – | – | – | – | – | – | – | – | – | – | 2378 | 1660.0 ± 17.1 | 1418 | 2650.0 ± 50.4 |
| 1995-05-27 | C204a | 1329-665 | – | – | – | – | – | – | 8640 | 347.0 ± 27.7 | 4800 | 855.0 ± 15.8 | – | – | – | – |
| 1995-05-27 | C204a | 1329-665 | – | – | – | – | – | – | 8640 | 347.0 ± 27.7 | 4800 | 855.0 ± 15.8 | – | – | – | – |
| 1995-06-07 | C204a | 1329-665 | – | – | – | – | – | – | 8640 | 348.0 ± 12.9 | 4800 | 853.0 ± 15.3 | – | – | – | – |
| 1995-06-07 | C204a | 1329-665 | – | – | – | – | – | – | 8640 | 348.0 ± 12.9 | 4800 | 853.0 ± 15.3 | – | – | – | – |
| 1995-07-27 | C204c | 1329-665 | – | – | – | – | – | – | – | – | – | – | 2368 | 1680.0 ± 15.1 | 1376 | 2860.0 ± 19.9 |
| 1995-08-03 | C363 | 1329-665 | – | – | – | – | – | – | – | – | – | – | – | – | 1418 | 2480.0 ± 82.3 |
| 1996-02-06 | CT09 | 1718-649 | – | – | – | – | – | – | – | – | – | – | – | – | 1664 | 3640.0 ± 61.4 |

*Note.* Column 1: starting date of observation. Column 2: observing programme ID. Column 3: calibrator. Columns 4, 6, 8, 10, 12, 14, and 16: mean frequency of observed band in units of MHz. Columns 5, 7, 9, 11, 13, 15, and 17: integrated flux densities in units of mJy as measured by UVFIT in MIRIAD.

**Table A2.** Nucleus.

| Obs. date | Obs. ID | *W* band | | $K_a$ band | | *K* band | | *X* band | | *C* band | | *S* band | | *L* band | |
|---|---|---|---|---|---|---|---|---|---|---|---|---|---|---|---|
| | | $\nu$ | $S_\nu$ | $\nu$ | $S_\nu$ | $\nu$ | $S_\nu$ | $\nu$ | $S_\nu$ | $\nu$ | $S_\nu$ | $\nu$ | $S_\nu$ | $\nu$ | $S_\nu$ |
| (1) | (2) | (3) | (4) | (5) | (6) | (7) | (8) | (9) | (10) | (11) | (12) | (13) | (14) | (15) | (16) |
| 1995-01-20 | C363 | – | – | – | – | – | – | – | – | – | – | – | – | 1418 | $45.8 \pm 2.9$ |
| 1995-02-25 | C363 | – | – | – | – | – | – | – | – | – | – | – | – | 1418 | $65.0 \pm 3.1$ |
| 1995-03-03 | C204a | – | – | – | – | – | – | 8640 | $22.7 \pm 9.0$ | 4800 | $44.9 \pm 4.3$ | – | – | – | – |
| 1995-03-03 | C204a | – | – | – | – | – | – | 8640 | $37.4 \pm 9.2$ | 4800 | $45.5 \pm 4.4$ | – | – | – | – |
| 1995-03-30 | C363 | – | – | – | – | – | – | – | – | – | – | – | – | 1418 | $64.3 \pm 2.3$ |
| 1995-04-16 | C418 | – | – | – | – | – | – | – | – | – | – | 2768 | $53.4 \pm 1.0$ | 1418 | $62.8 \pm 1.0$ |
| 1995-05-27 | C204a | – | – | – | – | – | – | 8640 | $41.1 \pm 11.0$ | 4800 | $48.8 \pm 4.9$ | – | – | – | – |
| 1995-05-27 | C204a | – | – | – | – | – | – | 8640 | $48.0 \pm 12.0$ | 4800 | $48.6 \pm 4.9$ | – | – | – | – |
| 1995-06-07 | C204a | – | – | – | – | – | – | 8640 | $48.7 \pm 12.0$ | 4800 | $43.2 \pm 4.3$ | – | – | – | – |
| 1995-06-07 | C204a | – | – | – | – | – | – | 8640 | $49.1 \pm 1.2$ | 4800 | $42.9 \pm 4.3$ | – | – | – | – |
| 1995-07-27 | C204c | – | – | – | – | – | – | – | – | – | – | 2368 | $44.5 \pm 3.5$ | 1376 | $65.8 \pm 4.0$ |

*Note.* Column 1: starting date of observation. Column 2: observing programme ID. Columns 3, 5, 7, 9, 11, 13, and 15: mean frequency of observed band in units of MHz. Columns 4, 6, 7, 10, 12, 14, and 16: integrated flux densities in units of mJy as measured by UVFIT or IMFIT in MIRIAD.

## SUPPORTING INFORMATION

Additional Supporting Information may be found in the online version of this article:

**Table 1.** ATCA Radio observations
**Table A1.** Calibrators
**Table A2.** Nucleus. (http://mnras.oxfordjournals.org/lookup/suppl/doi:10.1093/mnras/stt340/-/DC1).

Please note: Oxford University Press are not responsible for the content or functionality of any supporting materials supplied by the authors. Any queries (other than missing material) should be directed to the corresponding author for the article.

This paper has been typeset from a TEX/LATEX file prepared by the author.